

# A Novel Differential Pathlength Factor Model for Near-Infrared Diffuse Optical Imaging

KAISER NIKNAM,<sup>1</sup> MANNU BARDHAN PAUL,<sup>2</sup> AND MINI DAS<sup>1,2,3,\*</sup>

<sup>1</sup>*Department of Physics, University of Houston, Houston, TX, 77204, USA*

<sup>2</sup>*Department of Biomedical Engineering, University of Houston, Houston, TX, 77204, USA*

<sup>3</sup>*Department of Electrical and Computer Engineering, University of Houston, Houston, TX, 77204  
\*mdas@uh.edu*

**Abstract:** Near infrared diffuse optical imaging can be performed in reflectance and transmission mode and relies on physical models along with measurements to extract information on changes in chromophore concentration. Continuous-wave near-infrared diffuse optical imaging relies on accurate differential pathlength factors (DPFs) for quantitative chromophore estimation. Existing DPF definitions inherit formulation-dependent limitations that can introduce large errors in modified Beer–Lambert law analyses. These errors are significantly higher at smaller source–detector separations in a reflectance mode of measurement. This minimizes their applicability in situations where large area detection is used and also when signal depth is varying. Using Monte Carlo simulations, we derive two distance- and property-dependent DPF models—one ideal and one experimentally practical—and benchmark them against standard formulations. The proposed models achieve errors below 10% across broad optical conditions, whereas conventional DPFs can exceed 100% error. The theoretical predictions are further validated using controlled phantom experiments, demonstrating improved quantitative accuracy in CW-NIR imaging.

## 1. Introduction

Near-infrared (NIR) deep tissue imaging approaches have been extensively investigated as a complementary modality to radiological imaging, which often does not provide functional or molecular information. The utility of NIR imaging lies in the ability of near-infrared light to penetrate several centimeters into biological tissue, enabling real-time estimation of chromophore concentration changes—particularly those of oxyhemoglobin ( $\text{HbO}_2$ ) and deoxyhemoglobin (HHb) [1–5]. Time-domain (TD) NIR imaging methods rely on measuring the temporal point-spread function of ultrashort light pulses after propagation through tissue, from which absorption and scattering properties are inferred based on photon time-of-flight statistics [6–8]. Frequency-domain (FD) methods rely on detecting the amplitude attenuation and phase shift of intensity-modulated light after tissue propagation, which encode the tissue optical absorption and scattering characteristics [9–11]. However, continuous-wave near-infrared (CW-NIR) diffuse optical imaging methods are significantly simpler, more portable, and cost-effective.

In CW-NIR imaging, changes in detected light intensities measured at multiple time points and across a range of source–detector separations (in either reflectance or transmission mode) are used to map relative changes in tissue absorption associated with physiological variations. As a result, this modality is widely used to monitor tissue oxygenation and hemodynamics in both research and clinical settings [12–14]. It has found broad applications, including functional brain mapping [15, 16], muscle oxygenation monitoring during exercise [17, 18], and assessment of tissue viability under pathological conditions [19, 20]. In all of these methods, owing to the limited penetration depth of near-infrared photons (typically within the 650–900 nm optical window), reflectance–mode measurements are most commonly employed in practical imaging configurations. Photons detected at larger source–detector separations have, on average, sampled deeper tissue volumes, thereby providing increased sensitivity to subsurface physiological changes.

Inverse problems in all of these NIR deep tissue imaging require an estimation or approximation

of the true pathlength (for varying source–detector separations). The true pathlength is longer than the actual separation owing to multiple scattering within the tissue and thus depends on both tissue optical properties, geometry, and the source–detector separation. For media with higher scattering, the photons undergo a significantly higher number of scattering events before arriving at the detector either in transmission or reflectance mode of imaging. This scaling or increase in average photon pathlength in comparison to the actual linear source–detector distance is referred to as the differential pathlength factor (DPF). Estimation or modeling of DPF is critical in inverse problems related to NIR imaging.

The DPF concept was originally introduced by Delpy *et al.* as the ratio of the mean photon pathlength to the source–detector separation [2]. Since then, research on DPF estimation has centered on two major challenges: (1) accurately determining the true optical pathlength that photons travel in tissue, and (2) developing models of DPF that capture pathlength effects with sufficient accuracy for quantitative applications in the MBLL. To address the first challenge, a variety of experimental and computational approaches have been explored. Time-domain NIR spectroscopy employs ultrashort light pulses and measures photon time-of-flight distributions directly, providing detailed information on pathlength distributions across tissues and wavelengths [6–8]. Frequency-domain methods use intensity-modulated light and detect phase shifts and amplitude demodulation, from which the mean photon transit time—and thus the average pathlength—can be inferred *in vivo* [9–11]. These techniques enable absolute calibration of photon pathlength and precise quantification of DPF, but they require considerably more complex instrumentation and come at a substantially higher cost. Consequently, time- and frequency-domain systems remain far less common than CW systems. However, because CW instruments measure only steady-state attenuation, they cannot independently determine photon pathlength [21] and must instead rely on values obtained from those advanced modalities. In CW-NIR imaging, DPF values are often approximated or simple models are used. Errors in DPF measurements can cause significant inaccuracies in CW-NIR imaging.

In addition to experimental techniques, computational approaches such as Monte Carlo photon-transport simulations [22] and diffusion-equation models [23] have been employed to estimate pathlength factors under controlled conditions [24–33]. While these methods can predict photon pathlength distributions for specified optical properties and geometries, they rely on accurate knowledge of both tissue anatomy and optical coefficients. Consequently, inaccuracies in anatomical representation or in the assumed optical parameters (e.g., the use of generic head models or literature-averaged values) can cause simulation-based estimates to deviate substantially from actual *in vivo* or *in vitro* measurements.

The second challenge lies in integrating pathlength information into a practical DPF model for CW measurements. Early studies defined DPF simply as the ratio of mean optical pathlength to the source–detector distance [2]. However, Sassaroli *et al.* [31, 34] demonstrated that this definition is only partially correct, and instead proposed defining DPF as the slope of absorption-induced changes in optical density with respect to the absorption coefficient, normalized by the source–detector separation. Despite this, in practice, DPF is often approximated as a constant for source–detector separations exceeding 2.5 cm [9, 25, 35, 36]. This assumption is motivated by its simplicity and by the fixed separation typically used in CW-NIR measurements, leading the distance dependence of DPF to be neglected [13, 21, 37–42]. However, extensive evidence indicates that DPF is not invariant, but depends on tissue optical properties and photon pathlength characteristics [13, 37, 40]. Approximating DPF as a constant can therefore introduce substantial systematic errors in recovered chromophore concentrations, compromising quantitative accuracy [21, 39, 41, 42].

These considerations motivate the present study. We systematically examine how different definitions of the DPF influence the accuracy of absorption coefficient and chromophore concentration estimation in CW-NIR measurements. Using Monte Carlo photon–transport

simulations spanning a broad range of optical properties and source–detector separations, we evaluate several widely used DPF formulations and compare them directly with two alternative definitions introduced in this work. By applying each formulation to estimate the absorption coefficient in every simulation—where the ground-truth values are known—we assess the strengths and limitations of each approach. In addition to the simulation-based analysis, we experimentally confirm the validity of the proposed definitions using controlled phantom measurements. Our results demonstrate that the alternative definitions presented here yield highly accurate estimates across a broad range of optical properties and geometries, with consistent agreement between simulation and experiment. Collectively, these findings establish a practical framework that enhances the quantitative reliability of CW-NIR imaging, bridging experimental simplicity with quantitative rigor and advancing its potential for robust functional and clinical applications.

## 2. Methods

### 2.1. CW-NIR Imaging Models

Quantitative interpretation of CW-NIR measurements is governed by the modified Beer–Lambert law (MBLL), which extends the classical Beer–Lambert law to account for photon scattering in turbid media [2]. For a given source–detector separation  $d$ , chromophore concentration  $C$ , and wavelength  $\lambda$ , the measured optical density  $\text{OD}(C, d, \lambda)$  (absorbance) can be expressed as:

$$\text{OD}(C, d, \lambda) = -\log_{10} \frac{I_d}{I_0} = \mu_a(C, \lambda) \cdot d \cdot \text{DPF}(C, d, \lambda) \quad (1)$$

where  $I_0$  is the incident light intensity,  $I_d$  is the detected intensity at a distance  $d$  from the source,  $\mu_a(C, \lambda)$  is the absorption coefficient, and  $\text{DPF}(C, d, \lambda)$  is the differential pathlength factor. The DPF accounts for the elongation of photon trajectories due to scattering, effectively scaling the geometric separation  $d$  to the true mean optical pathlength,  $s$ , between source and detector. Reported DPF values range from about 1 up to 16 (most commonly between 3 and 6 [21]), depending on tissue type, wavelength, and measurement geometry [2, 36, 42–44]. In general, the DPF increases with source–detector separation and with higher scattering coefficients ( $\mu_s$ ). Although the absorption coefficient does not directly determine the mean photon pathlength, greater absorption preferentially attenuates longer photon trajectories, thereby shortening the effective pathlength and reducing the measured DPF. The absorption coefficient is related to the chromophore concentration through the molar extinction coefficient  $\varepsilon(\lambda)$ :

$$\mu_a(C, \lambda) = \varepsilon(\lambda) \cdot C \quad (2)$$

Together, Eqs. (1) and (2) emphasize the role of DPF as a critical scaling factor that links measured optical attenuation to the underlying chromophore concentrations.

### 2.2. Existing DPF Models

The differential pathlength factor was originally introduced as the **mean-pathlength DPF**, which scales the geometric source–detector distance to the mean optical pathlength traveled by photons, thereby accounting for the elongation of photon trajectories caused by multiple scattering [2, 6, 9, 36, 45]. It is formally defined as

$$\text{DPF}_{\text{mean}}(d) = \frac{\bar{s}(d)}{d} \quad (3)$$

where  $\bar{s}(d)$  denotes the mean pathlength of photons detected at a source–detector separation  $d$ . As expected increases with both source–detector separation and the scattering coefficient  $\mu_s$ . A variety of studies have applied this formulation to estimate DPF by employing experimental or computational strategies to explicitly quantify the mean optical pathlength. Experimentally,

Duncan *et al.* utilized phase-resolved spectroscopy to directly measure photon transit times, converting these into absolute pathlength values to establish reference DPFs for the adult head and calf [9]. Similarly, Essenpreis *et al.* employed time-resolved spectroscopy to characterize the wavelength dependence of the DPF [6]. Complementing these experimental efforts, computational studies have calculated the mean pathlength by statistically aggregating photon trajectories within complex tissue geometries; for instance, Althobaiti used Monte Carlo simulations to determine pathlength scaling specifically for the multi-layered architecture of human skin [45], while Chatterjee *et al.* applied similar transport modeling to investigate pathlength variations in reflectance photoplethysmography [36].

Although conceptually intuitive, the mean-pathlength formulation neglects absorption-weighted photon statistics and therefore tends to overestimate the effective optical pathlength in highly absorbing tissues, leading to systematic errors in DPF estimation. To address this limitation, Sassaroli *et al.* [34] proposed a **slope-based DPF**, defined as

$$\text{DPF}_{\text{slope}}(d) = \frac{1}{d} \cdot \frac{d(\text{OD}_d)}{d\mu_a} \quad (4)$$

where  $\text{OD}_d$  denotes the optical density measured at a source–detector separation  $d$ . This definition has been widely adopted because it provides a theoretically grounded means of estimating DPF directly from intensity measurements, thereby obviating the need for explicit knowledge of individual photon pathlengths. In analytical studies, Ultman and Piantadosi demonstrated that the derivative of optical attenuation with respect to absorption accurately captures the effective pathlength in diffusive media [35]. Experimental validation was provided by Kohl *et al.*, who applied the slope-based approach to cortical measurements and showed close agreement between intensity-derived DPF estimates and values obtained using phase-resolved spectroscopy [37]. Furthermore, computational investigations have leveraged this definition to evaluate optical sensitivity in complex biological environments; for example, Alexander *et al.* employed Monte Carlo simulations to assess pathlength variations in a mouse model of Alzheimer’s disease [39], while Bhatt *et al.* extended the framework to thick, heterogeneous tissues to better account for spatial variations in optical properties [31].

Incorporating the slope-based definition into the diffusion-equation framework yields an analytical expression for the DPF in a semi-infinite slab with homogeneous absorption and scattering coefficients. This formulation, referred to as the **semi-infinite DPF**, is given by [23, 26, 44]:

$$\text{DPF}_{\text{seminf}} = \frac{1}{2} \sqrt{\frac{3\mu_s(1-g)}{\mu_a}} \cdot \left[ 1 - \frac{1}{1 + d\sqrt{3\mu_s(1-g)\mu_a}} \right] \quad (5)$$

where  $g$  denotes the scattering anisotropy factor. Within this semi-infinite geometry, the DPF increases with the source–detector separation  $d$  before approaching an asymptotic value. For typical tissue optical properties, this saturation occurs once  $d$  exceeds approximately 0.5–0.7 cm [23]. Consequently, for separations larger than 2.5 cm, the DPF is frequently approximated as invariant [25]. Based on this asymptotic behavior, a **constant DPF** has been proposed and remains widely adopted in practice. It is defined as the limiting case of Eq. 5 as  $d \rightarrow \infty$  [23, 39–41, 43, 44, 46]:

$$\text{DPF}_{\text{constant}} = \frac{1}{2} \sqrt{\frac{3\mu_s(1-g)}{\mu_a}} \quad (6)$$

The constant DPF formulation is extensively employed to quantify chromophore concentrations in deep-tissue measurements. By treating the pathlength factor as invariant within this asymptotic

regime, measured attenuation changes can be directly converted into chromophore concentration estimates without requiring real-time pathlength monitoring. Fantini *et al.*, for example, applied this approach to assess cerebral oxygenation in neonates [23], while Chiarelli *et al.* employed it in high-density adult recordings to mitigate hemoglobin cross-talk [46]. Although this simplification is standard in skeletal muscle oximetry [41], its accuracy depends critically on the stability of tissue optical properties; indeed, Ferreira *et al.* cautioned that assuming a fixed scattering coefficient—implicit in the constant DPF definition—can introduce errors during dynamic physiological conditions such as muscle contraction [43].

### 2.3. Computational Framework

To evaluate the limitations of existing DPF formulations and to guide the development of improved alternatives, we performed a series of Monte Carlo photon-transport simulations spanning a broad range of absorption and scattering coefficients representative of biological tissue. For each condition, the simulated optical density was combined with each DPF formulation to estimate the absorption coefficient, whose ground-truth value was known *a priori*. This framework enabled a direct and quantitative assessment of estimation errors across all DPF models.

Simulations were performed using MCmatlab [47], assuming a homogeneous tissue-slab geometry of  $29 \times 29 \times 5 \text{ cm}^3$ . The slab dimensions were intentionally chosen to approximate a semi-infinite medium. In each simulation, approximately one million photons were launched from a pencil-beam light source positioned at the center of the slab's top surface (Fig. 1a). The absorption coefficient,  $\mu_a$ , was varied from 0 to  $0.5 \text{ cm}^{-1}$  in increments of  $0.05 \text{ cm}^{-1}$ , while the scattering coefficient,  $\mu_s$ , ranged from 0 to  $500 \text{ cm}^{-1}$  in steps of  $50 \text{ cm}^{-1}$ . The anisotropy factor  $g$  was fixed at 0.95. As illustrated in the bottom panels of Fig. 1, photon trajectories varied markedly with the medium's optical properties. Increasing the scattering coefficient caused photons to exit closer to the source ( $< 1 \text{ cm}$ ) owing to enhanced scattering, whereas lower  $\mu_s$  values allowed photons to travel farther before exiting (compare Fig. 1c with Fig. 1b, and Fig. 1e with Fig. 1d). Similarly, higher absorption coefficients led to stronger attenuation, reducing the number of photons reaching the surface (compare Fig. 1d&e with Fig. 1b&c).

For each simulation, photon trajectories were recorded to determine the total pathlength traveled prior to absorption or escape from the medium. For photons exiting the top surface, additional quantities, including the exit location and exit weight, were stored. These data were used to compute the incident intensity ( $I_0$ ), the detected intensity ( $I_d$ ), and the corresponding

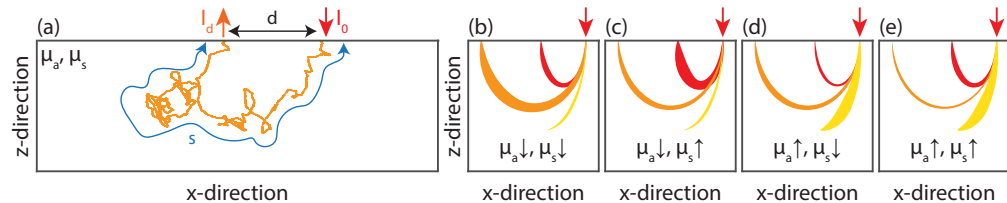


Fig. 1. (a) Schematic of the Monte Carlo simulation. One million photons were launched into a homogeneous tissue slab using a pencil-beam source (red arrow), and their trajectories (orange) were recorded. The trajectory data were used to determine each photon's pathlength  $s$ , source-detector separation  $d$ , and corresponding detected intensity (orange arrow). (b–e) Representative photon trajectories for different combinations of optical properties: (b) low  $\mu_a$ , low  $\mu_s$ ; (c) low  $\mu_a$ , high  $\mu_s$ ; (d) high  $\mu_a$ , low  $\mu_s$ ; and (e) high  $\mu_a$ , high  $\mu_s$ . Red, orange, and yellow traces denote photons that exited the top surface near the source ( $< 1 \text{ cm}$ ), exited farther from the source ( $> 1 \text{ cm}$ ), or were absorbed within the medium, respectively. The thickness of each trajectory bundle is proportional to the number of photons following that path.

optical density ( $OD_d$ ).

The incident intensity was defined as the total launched optical power per unit area. Assuming the launch of  $M$  photons (with  $M = 10^6$  in this study), each initialized with unit weight and reference power  $P_0$ , the incident intensity was computed as [47, 48]

$$I_0 = \frac{MP_0}{\pi\Delta^2} \quad (7)$$

where  $\Delta$  denotes the radial discretization step, and  $\pi\Delta^2$  corresponds to the area of the central circular bin associated with the normally incident pencil-beam source. The detected intensity at a source-detector separation  $d$  was obtained by summing the exit powers of all photons escaping through an annular detection bin spanning radii  $d - \Delta/2$  to  $d + \Delta/2$ , and normalizing by the corresponding annular area,

$$I(d) = \frac{\sum_{i=1}^{N_d} P_0 w_i}{2\pi d \Delta} \quad (8)$$

where  $w_i$  denotes the exit weight of photon  $i$ , and  $N_d$  is the total number of photons exiting within the detection annulus.

The optical density at distance  $d$  was then calculated as

$$OD_d = -\log_{10} \left( \frac{\Delta}{2Md} \sum_{i=1}^{N_d} w_i \right) \quad (9)$$

Because the discretization step  $\Delta$  enters both the incident and detected intensities solely as a constant normalization factor, variations in  $\Delta$  produce a uniform vertical shift in the optical density values, without affecting relative contrast, distance-dependent trends, or the generality of the analysis. In this study,  $\Delta = 2$  mm.

The weight of each photon attenuates exponentially with the distance traveled. A photon  $i$  that traverses a total pathlength  $s_i$  within the medium exits with weight  $w_i = \exp(-\mu_a s_i)$ , where  $\mu_a$  is the absorption coefficient of the medium. Substituting this relation into Eq. 9 yields

$$OD_d = -\log_{10} \left( \frac{\Delta}{2Md} \sum_{i=1}^{N_d} \exp(-\mu_a s_i) \right) \quad (10)$$

#### 2.4. Comparison Of Existing DPF Models With The Proposed Novel DPF Definitions

Using the quantities obtained from the Monte Carlo simulations, the various DPF formulations were computed for each combination of absorption and scattering coefficients ( $\mu_a, \mu_s$ ) in the simulated medium. Specifically, the mean-pathlength DPF was calculated as

$$DPF_{\text{mean}}(d) = \frac{\bar{s}(d)}{d} \quad (11)$$

where  $\bar{s}(d)$  denotes the arithmetic mean of the photon pathlengths for photons detected at a source-detector separation  $d$  within the defined collection annulus, given by

$$\bar{s}(d) = \frac{1}{N_d} \sum_{i=1}^{N_d} s_i$$

By combining Eqs. 10 and 4, the slope-based DPF was computed explicitly as

$$DPF_{\text{slope}}(d) = \frac{1}{d \ln 10} \frac{\sum_{i=1}^{N_d} s_i \exp(-\mu_a s_i)}{\sum_{i=1}^{N_d} \exp(-\mu_a s_i)} \quad (12)$$

The semi-infinite and constant DPF values were computed using the absorption and scattering coefficients ( $\mu_a, \mu_s$ ) assigned to each simulation, enabling direct comparison of all DPF formulations under identical optical conditions.

As stated earlier, the mean-pathlength DPF systematically overestimates the effective photon pathlength because it neglects absorption-weighted photon statistics. The slope-based formulation—and, by extension, the semi-infinite and constant DPF models derived from it—was introduced to mitigate this limitation by incorporating attenuation-weighted averaging. However, these formulations remain fundamentally focused on estimating an average photon trajectory, rather than directly addressing the primary objective of CW-NIR imaging, namely the accurate estimation of absorption coefficients and chromophore concentration changes.

To address this limitation, we define the DPF directly from the modified Beer–Lambert law by rearranging Eq. 1, yielding

$$\text{DPF}_{\text{true}}(d) = \frac{1}{d} \frac{\text{OD}_d}{\mu_a} \quad (13)$$

Substituting the Monte Carlo expression for the optical density into this relation yields the **true DPF**,

$$\text{DPF}_{\text{true}}(d) = -\frac{1}{d \mu_a} \log_{10} \left( \frac{1}{M} \sum_{i=1}^{N_d} \exp(-\mu_a s_i) \right) \quad (14)$$

This formulation fully captures the statistical nature of photon transport in absorbing, scattering media, demonstrating that an exponentially weighted pathlength average is physically superior to the arithmetic averaging inherent in the mean-pathlength and slope-based approximations.

Although the true DPF, defined directly from the full photon pathlength distribution, represents the theoretical gold standard, its computation requires explicit knowledge of individual photon trajectories and is therefore computationally prohibitive for routine experimental or clinical use. To bridge this gap between physical rigor and computational efficiency, we propose a new DPF model below.

Our new formulation (in Eqs. 17 and 18 below) is motivated by the observation that, although the dependence of optical density on source–detector separation  $d$  is inherently nonlinear, it can be accurately approximated over physiologically relevant distances by a linear combination of  $d$  and  $\log_{10}(d)$  with a nonzero intercept. This observation is rooted in classical diffusion-theory analyses. In particular, Farrell *et al.* [49] and subsequent studies [46, 50, 51] showed that, for a homogeneous semi-infinite scattering medium, the spatially resolved diffuse reflectance can be approximated as

$$\frac{I_d}{I_0} \propto \frac{1}{d^m} \exp(-C_1 d) \quad (15)$$

where the exponential term captures absorption-dominated attenuation and the power-law prefactor accounts for geometric photon spreading ( $m$  and  $C_1$  are medium-dependent constants determined by scattering and absorption). Taking the negative base-10 logarithm of the reflectance yields (see Eq. 1)

$$\text{OD}_d \approx \frac{C_1}{\ln 10} d + m \log_{10}(d) + \text{const} \quad (16)$$

demonstrating that OD naturally decomposes into a linear term in  $d$ , a logarithmic correction, and a nonzero offset arising from boundary conditions, source normalization, and finite scattering effects.

Monte Carlo simulations performed in this study confirm the validity of this approximation across a wide range of absorption and scattering coefficients. Fig. 2a shows representative OD profiles as a function of source–detector separation  $d$  (solid curves) for multiple ( $\mu_a, \mu_s$ ) combinations. When expressed in the mixed coordinate basis  $\{d, \log_{10}(d)\}$ , these profiles are well described by linear regressions (dashed curves). Importantly, the dashed fits in Fig. 2a

exhibit a consistent nonzero intercept, indicating that the effective optical pathlength cannot be fully captured by slope-only or purely proportional models. This intercept reflects residual photon path contributions that persist even at small separations and would be systematically neglected in conventional DPF formulations. The close agreement between the simulated OD curves (solid lines) and their linear approximations (dashed lines) demonstrates that the essential transport physics governing photon migration is preserved by this mixed linear representation.

Based on this empirical and theoretical insight, we formalize the relationship into an explicit **inverse-distance DPF** model that retains analytical simplicity while improving accuracy in concentration recovery. The proposed model is given by (combining Eqs. 13 and 16)

$$\text{DPF}_{\text{inv}}(d) = A + \frac{B}{d} + \frac{C \log_{10}(d)}{d}, \quad (17)$$

where  $A$ ,  $B$ , and  $C$  are regression coefficients obtained by fitting numerically or experimentally derived values of  $\text{OD}_d/\mu_a$  to the linear form

$$\frac{\text{OD}_d}{\mu_a} \approx A d + B + C \log_{10}(d). \quad (18)$$

Unlike the true DPF, which must be recomputed for each discrete separation, the inverse-distance formulation provides a continuous analytical description valid across the entire spatial domain. As a result, knowledge of only three parameters,  $A$ ,  $B$ , and  $C$ , is sufficient to determine the DPF at arbitrary source-detector separations. Furthermore, we demonstrate that  $A$ ,  $B$ , and  $C$  exhibit smooth and predictable dependencies on absorption and scattering coefficients—and by extension, chromophore concentrations—enabling robust empirical calibration across a wide physiological range.

Fig. 2b compares the resulting inverse-distance DPF values obtained from Eq. (17) with the corresponding true DPF values computed directly from photon pathlength statistics. Across all optical property combinations examined, the proposed model demonstrates close agreement with the true DPF, capturing both its magnitude and distance dependence with minimal deviation.

In summary, the six DPF models (including our proposed true and inverse-distance DPF models) considered here for comparison differ fundamentally in both their theoretical basis and computational complexity. The constant and semi-infinite formulations provide pragmatic but simplified approximations suitable for specific geometric regimes. The mean-pathlength and slope-based definitions are more physically motivated but fail to fully incorporate absorption-weighted photon statistics in the context of concentration estimation. The true DPF offers the most rigorous and physically consistent formulation, albeit at substantial computational cost. Finally, the inverse-distance DPF introduced in this work achieves an optimal balance between accuracy and efficiency by approximating the true DPF through a simple analytical expression.

Simulated optical density values were subsequently used to estimate the absorption coefficient using each of the six DPF models. Estimation accuracy was quantified across a broad range of source-detector separations and optical property combinations by calculating the relative error

$$e = \frac{\mu_{a,e} - \mu_a}{\mu_a} \times 100\%, \quad (19)$$

where  $\mu_{a,e}$  and  $\mu_a$  denote the estimated and true absorption coefficients, respectively.

## 2.5. Experimental Validation

In addition to Monte Carlo simulations, a tissue-mimicking phantom experiment was conducted using a CW-NIR setup to validate the findings in a physical setting. Two homogeneous scattering phantoms were prepared using a water-based super-absorbent polymer (SAP) hydrogel matrix (diaper polymer; Science Gone Fun, E-N Corp., Redford, MI, USA) mixed with titanium dioxide

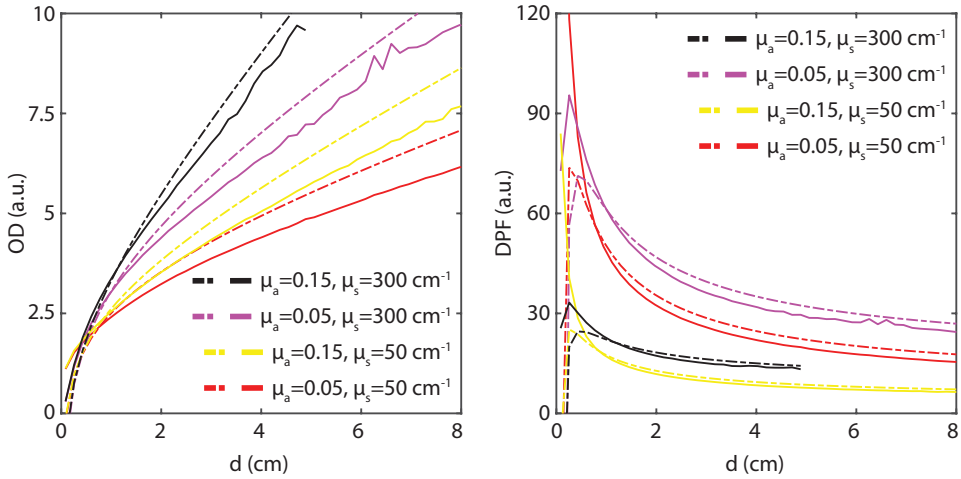


Fig. 2. (a) Optical density as a function of source–detector separation  $d$  for representative combinations of absorption and scattering coefficients ( $\mu_a, \mu_s$ ). Solid curves show Monte Carlo–derived OD values. Dashed curves represent fits of the same data to the mixed linear model given in Eq. 18, demonstrating that the simulated OD profiles are well approximated by a linear combination of  $d$  and  $\log_{10}(d)$  with a nonzero intercept. (b) Comparison of the corresponding true DPF values (solid curves), computed directly from photon pathlength statistics, with the inverse-distance DPF estimates (dashed curves) obtained using Eq. (17).

( $\text{TiO}_2$ ) powder. This composition was selected to provide a stable, repeatable scattering medium with negligible intrinsic absorption, allowing for controlled optical property manipulation. The phantoms were cast in an acrylic mold with dimensions  $15 \times 15 \times 6 \text{ cm}^3$ , providing a volume of approximately 1.35 L to approximate a semi-infinite medium. The scattering agent consisted of  $\text{TiO}_2$  powder (nominal particle size  $44 \mu\text{m}$ ; Loudwolf Industrial & Scientific, Dublin, CA, USA) dispersed in tap water. Both phantoms contained a SAP concentration of approximately 7 g/L, with  $\text{TiO}_2$  concentrations of 0.25 mg/mL and 1.0 mg/mL, respectively.

The experimental setup utilized a light-emitting diode (LED) with a peak wavelength of 750 nm (LED750L, Thorlabs, Newton, NJ, USA) to probe the phantom. The LED, housed in a TO-18 package with a spherical glass lens providing a narrow viewing angle ( $\pm 11^\circ$ ), was driven by a stable 5 V DC supply in series with a current-limiting resistor ( $150 \Omega$ ) to ensure constant optical output. Detection was performed using a silicon photodiode (FDS100, Thorlabs, Newton, NJ, USA) with an active area of  $13 \text{ mm}^2$ , operating in a photovoltaic mode with a transimpedance amplifier circuit. The analog voltage signal, proportional to the detected light intensity, was digitized using an Arduino Mega 2560 microcontroller (Arduino, LLC) and recorded on a host computer (Fig. 3).

Measurements were performed in a diffuse reflectance geometry. The source and detector were positioned on the phantom surface using a custom lid containing a  $13 \times 13$  grid of holes with a 1 cm pitch (Fig. 3). The LED was fixed at the center hole, and the detector was swept across the remaining grid positions. This configuration allowed the source–detector separation to be varied discretely from 1 cm to approximately 8.5 cm (center-to-corner distance). For each separation distance, the optical density was calculated as  $\text{OD}_d = -\log_{10}(I_d/I_0)$ . The detected intensity  $I_d$  was derived from the measured photodiode voltage, while the incident source intensity  $I_0$  was estimated from the voltage–optical power characteristic curves of the light-emitting diode and independently confirmed through a controlled pre-measurement to ensure the validity of this

theoretical assumption.

To evaluate the accuracy of the proposed differential pathlength factor models across different scattering regimes, reference optical properties—absorption coefficient  $\mu_a$ , scattering coefficient  $\mu_s$ , and anisotropy factor  $g$ —were derived from literature values for titanium-dioxide-based tissue-mimicking phantoms [52] corresponding to the specific concentrations used (0.25 mg/mL and 1.0 mg/mL). Table 1 summarizes the values obtained for these phantoms. These parameters were utilized to configure separate Monte Carlo simulations for each phantom. This approach served two purposes: first, to validate the experimental optical density trends against theoretical predictions for both scattering densities, and second, to compute the theoretical mean optical pathlength of photons in each medium. The resulting pathlength data enabled the calculation of the standard differential pathlength factor models (mean-pathlength, true, etc.), which were then applied to the respective experimental optical density data to estimate the absorption coefficient and quantify relative errors.

Table 1. Assigned optical properties of the homogeneous super-absorbent polymer–titanium dioxide phantoms at 750 nm based on literature values [52].

TiO <sub>2</sub> concentration	Refractive index	$\mu_a$ (cm <sup>-1</sup> )	$\mu_s$ (cm <sup>-1</sup> )	$g$
0.25 mg/mL	1.33	0.0275	8.75	0.93
1.00 mg/mL	1.33	0.0275	35.0	0.93

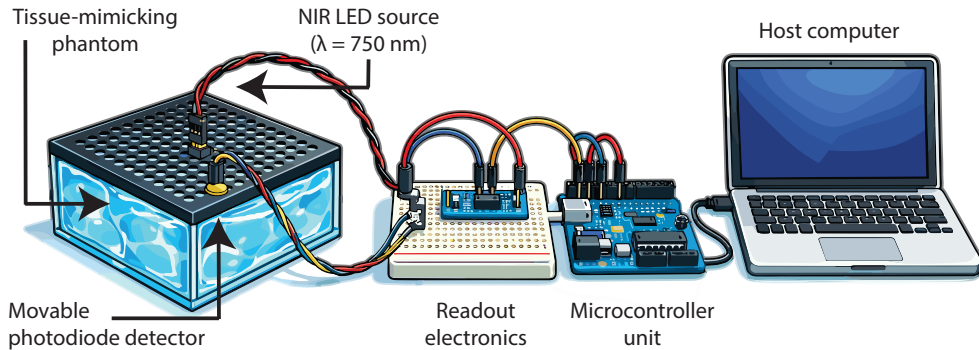


Fig. 3. Experimental setup for validation using a homogeneous tissue-mimicking phantom. The phantom consists of a water-based super-absorbent polymer hydrogel matrix mixed with titanium dioxide particles and cast in a 15 × 15 × 6 cm<sup>3</sup> acrylic mold. A fixed 750 nm light-emitting diode source illuminates the phantom surface at the center of a 13 × 13 measurement grid with a 1 cm pitch, while a movable silicon photodiode detector samples diffuse reflectance at varying source–detector separations. The detected signal is conditioned by readout electronics, digitized by a microcontroller unit, and recorded on a host computer.

### 3. Results & Discussion

We systematically examined the behavior of the six DPF models across a wide range of source–detector separations and optical properties to evaluate their impact on the accuracy of absorption coefficient estimation. Figure 4 (left panel) illustrates the variation of each DPF definition as a function of source–detector separation for a representative set of optical properties ( $\mu_a = 0.15$  cm<sup>-1</sup>,  $\mu_s = 50$  cm<sup>-1</sup>). The true DPF and the inverse-distance DPF model

exhibit remarkable agreement across most of the separation range, indicating that the proposed analytical approximation closely reproduces the pathlength statistics obtained from photon-resolved simulations. In contrast, the mean-pathlength, slope-based, and semi-infinite DPF formulations display nearly identical behavior and, together with the constant DPF, consistently underestimate the true pathlength factor.

The right panel of Fig. 4 quantifies the corresponding relative error in estimating the absorption coefficient for each DPF model across source-detector separations ranging from 0 to 8 cm. As expected, the true DPF yields negligible error across all distances. The inverse-distance DPF model also demonstrates high accuracy, maintaining relative errors below 10% over the majority of the separation range. Conversely, the constant, mean-pathlength, slope-based, and semi-infinite DPF formulations exhibit the poorest performance, producing substantial errors that frequently exceed 100%. Notably, while the estimation errors associated with the mean-pathlength and slope-based DPFs do not exhibit a consistently decreasing trend with increasing separation, the constant and semi-infinite DPFs display a trend suggesting improved performance at very large separations ( $> 8$  cm), a regime that lies beyond the practical operating range of many continuous-wave systems.

These trends persist across a broad parameter space, with absorption coefficients  $\mu_a$  ranging from 0 to  $0.5 \text{ cm}^{-1}$  and scattering coefficients  $\mu_s$  ranging from 0 to  $500 \text{ cm}^{-1}$ . Across all optical property combinations examined, the true DPF consistently yields zero estimation error, while the mean-pathlength, slope-based, semi-infinite, and constant DPF formulations produce errors exceeding 100% at most source-detector separations.

Figure 5a depicts the absolute relative error associated with the constant DPF model, shown here as a representative example of the previously proposed simplified DPF formulations. Errors are averaged over source-detector separations ranging from 1 to 8 cm. This interval was selected to maximize clinical relevance: separations below 1 cm provide insufficient depth sensitivity for deep-tissue interrogation, while separations exceeding 8 cm generally surpass the effective detection limits of current continuous-wave near-infrared systems. The results

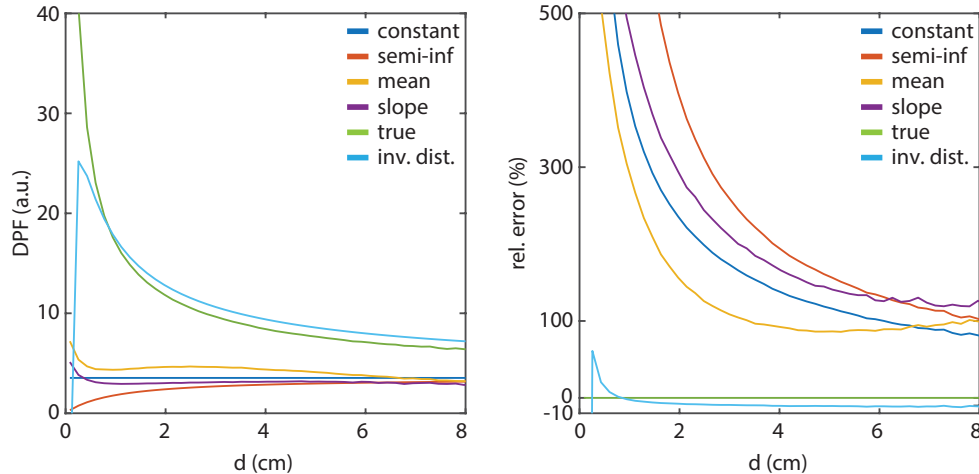


Fig. 4. Comparison of DPF models and their corresponding absorption coefficient estimation errors for a representative optical property pair ( $\mu_a = 0.15 \text{ cm}^{-1}$ ,  $\mu_s = 50 \text{ cm}^{-1}$ ). (Left) Variation of the DPF as a function of source-detector separation for the constant, semi-infinite, mean-pathlength, slope-based, true, and inverse-distance models. (Right) Relative error in estimating the absorption coefficient using each DPF formulation as a function of source-detector separation.

demonstrate that the constant DPF model maintains average errors exceeding 100% across regions of lower absorption and scattering, which correspond to the typical optical properties of biological tissues [53]. In contrast, Fig. 5b depicts the absolute relative error obtained using the inverse-distance DPF model, averaged over the same source-detector separation range. The inverse-distance model maintains an average error below 5% across the majority of the optical property space. Crucially, this high level of accuracy is particularly robust within regions of lower absorption and scattering, which are most representative of biological tissues encountered in near-infrared spectroscopy applications.

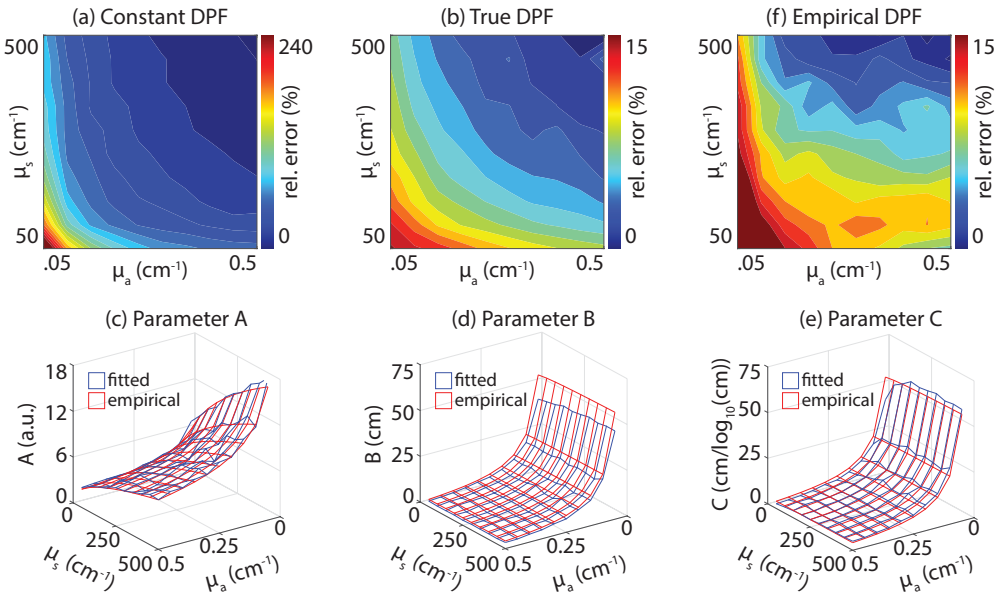


Fig. 5. (a) Average absolute relative error in estimating the absorption coefficient using the constant DPF model as a function of absorption and scattering coefficients. Errors are averaged over source-detector separations between 1 and 8 cm. (b) Average absolute relative error obtained using the true DPF under the same conditions. (c–e) Variation of the inverse-distance DPF parameters  $A$  (panel c),  $B$  (panel d), and  $C$  (panel e) across the  $\mu_a$ – $\mu_s$  space, comparing empirically fitted values with regression-derived values. (f) Average absolute relative error obtained using the fully empirical inverse-distance DPF model.

Although the parameters  $A$ ,  $B$ , and  $C$  of the inverse-distance DPF model are obtained through linear regression, their dependence on the absorption and scattering coefficients is smooth and well behaved across the entire optical property space investigated (Fig. 5c–e). Based on these observations, the following empirical relationships were derived:

$$A \approx 0.33 \times \mu_a^{-0.43} \times \mu_s^{0.43}, \quad (20)$$

$$B \approx 1.21 \times \mu_a^{-1.19} \times \mu_s^{0.02}, \quad (21)$$

$$C \approx 0.70 \times \mu_a^{-1.16} \times \mu_s^{0.18}. \quad (22)$$

These expressions closely reproduce the regression-derived parameters, with coefficients of determination approaching unity for all three parameters. Figure 5c–e illustrates the comparison between empirically fitted and regression-derived values of  $A$ ,  $B$ , and  $C$  across the  $\mu_a$ – $\mu_s$  space, demonstrating excellent agreement. Using Eqs. 17, 20, 21, and 22, we constructed a fully

empirical DPF model. Figure 5f presents the corresponding average absolute relative error, again averaged over source-detector separations between 1 and 8 cm. The empirical model reproduces the performance of the inverse-distance formulation while eliminating the need for additional simulations or experimental calibration.

To verify the simulation-based findings in a physical setting, we analyzed the diffuse reflectance data acquired from the two  $\text{TiO}_2$  phantoms (0.25 mg/mL and 1.00 mg/mL). Figure 6a compares the experimentally measured optical density with Monte Carlo predictions initialized using literature-derived optical properties. The experimental measurements (symbols) exhibit excellent agreement with the Monte Carlo results (solid lines) across the full range of source-detector separations for both phantom concentrations. This close correspondence validates the experimental setup as well as the accuracy of the assumed optical properties, thereby establishing a reliable baseline for evaluating the performance of the DPF models. This validation step is essential, as accurate photon pathlength distributions—derived here from the validated simulations—are required to compute the true, mean-pathlength, and slope-based DPFs.

Using the experimental optical density data, the absorption coefficients of both phantoms were subsequently estimated employing all six DPF formulations. Figures 6b and 6c present the relative estimation errors for the 0.25 mg/mL and 1.00 mg/mL phantoms, respectively. In agreement with the numerical results, both the true and inverse-distance DPF models demonstrate acceptable accuracy, maintaining relative errors below 20% across the measured source-detector separation range. In contrast, the conventional DPF models, including the slope-based, semi-infinite, and constant formulations, exhibit pronounced inaccuracies, particularly at short separations, where estimation errors frequently exceed 100%. Although these traditional models show moderate improvement at larger separations, they consistently underperform relative to the true and inverse-distance DPF models.

Overall, these experimental findings corroborate the simulation-based conclusions and confirm that the true and inverse-distance DPF formulations more accurately capture the separation-dependent photon pathlength scaling. Consequently, they provide a robust and physically consistent alternative to conventional DPF approximations when applied to realistic tissue-mimicking environments.

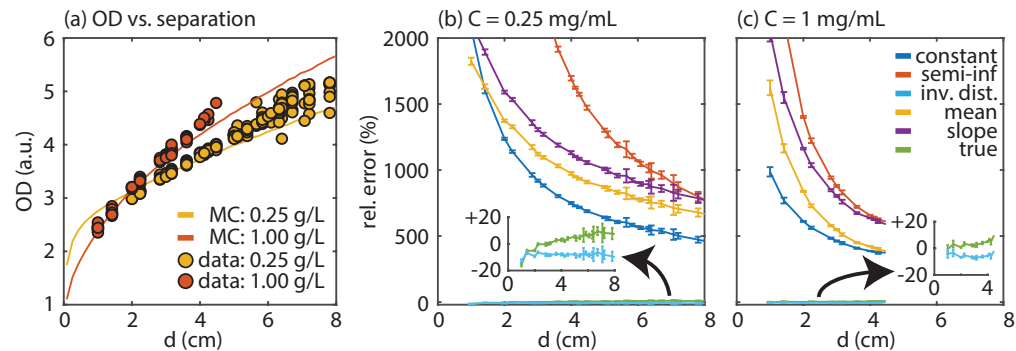


Fig. 6. (a) Experimental validation of optical density as a function of source-detector separation. Measured optical density values (circles) for homogeneous phantoms with  $\text{TiO}_2$  concentrations of 0.25 mg/mL (yellow) and 1.00 mg/mL (red) are compared with Monte Carlo predictions (solid lines). (b, c) Relative error in estimating the absorption coefficient for the (b) 0.25 mg/mL and (c) 1.00 mg/mL phantoms using six different DPF formulations. Error bars indicate the standard deviation of the estimation error.

#### 4. Conclusion

Accurate estimation of the DPF is essential for reliable chromophore concentration measurements in CW-NIR diffuse optical imaging. In this study, we performed a systematic evaluation of four commonly used DPF formulations and introduced both the ideal true DPF, which provides the highest achievable accuracy, and a practical inverse-distance DPF model designed to balance physical accuracy with computational efficiency. As expected, the true DPF yielded ideal performance and served as the theoretical gold standard. The proposed inverse-distance DPF closely approximated the true DPF across a wide range of optical properties and source-detector separations, while offering a substantial reduction in computational complexity. In contrast, the constant, mean-pathlength, and slope-based DPF formulations consistently underperformed across all tested regimes, often producing large estimation errors.

Importantly, the simulation-based findings were independently validated through controlled tissue-mimicking phantom experiments. The experimentally measured optical density trends and absorption coefficient estimates closely matched the Monte Carlo predictions, confirming that the observed performance differences among DPF models persist in a physical measurement setting. This experimental confirmation strengthens the generality and practical relevance of the conclusions drawn from the numerical analysis.

Our results highlight the critical importance of accurate DPF modeling, particularly at short source-detector separations where detected signal levels are highest and measurement precision is greatest. In this regime, inaccuracies in DPF modeling directly translate into substantial errors in absorption coefficient estimation. At larger separations, although some simplified DPF models exhibit modest improvements, the reduced signal-to-noise ratio ultimately limits concentration accuracy regardless of the DPF formulation employed.

Overall, these findings underscore the practical utility of refined DPF formulations such as the inverse-distance model. While minor deviations from the true DPF are observed at very short separations, these discrepancies are of limited practical concern due to the dominant sensitivity of such measurements to superficial tissue layers. Consequently, the inverse-distance DPF provides a robust and efficient alternative to conventional models and is well suited for routine use in CW-NIR diffuse optical imaging, where rapid and reliable concentration estimation is required.

Future work will focus on extending this framework to heterogeneous tissue structures, for which the partial pathlength factor (PPF) provides a more appropriate metric than the DPF. In addition, although the present study is restricted to CW-NIR systems, adapting the proposed modeling strategy to time-domain and frequency-domain modalities will be explored. Such extensions will require dedicated approaches to account for the distinct photon transport dynamics inherent to these techniques. Ultimately, these developments may enable more accurate and robust quantification of tissue optical properties in both research and clinical applications, thereby enhancing the diagnostic and monitoring capabilities of diffuse optical imaging.

**Funding.** National Institute of Biomedical Imaging and Bioengineering (R01 EB029761); Congressionally Directed Medical Research Programs (BC151607); National Science Foundation (1652892).

**Acknowledgments.** The authors acknowledge the use of the Carya Cluster and the advanced support provided by the Research Computing Data Core at the University of Houston in carrying out the research presented in this study.

**Disclosures.** The authors declare no conflicts of interest.

**Data availability.** Data underlying the results presented in this study are not publicly available at this time but may be obtained from the authors upon reasonable request.

#### References

1. F. Scholkmann, S. Kleiser, A. J. Metz, *et al.*, “A review on continuous wave functional near-infrared spectroscopy and imaging instrumentation and methodology,” *NeuroImage* **85**, 6–27 (2014).

2. D. T. Delpy, M. Cope, P. van der Zee, *et al.*, “Estimation of optical pathlength through tissue from direct time of flight measurement,” *Phys. Med. & Biol.* **33**, 1433–1442 (1988).
3. M. S. Patterson, B. Chance, and B. C. Wilson, “Time resolved reflectance and transmittance for the noninvasive measurement of tissue optical properties,” *Appl. Opt.* **28**, 2331–2336 (1989).
4. E. M. Sevick, B. Chance, J. Leigh, *et al.*, “Quantitation of time- and frequency-resolved optical spectra for the determination of tissue oxygenation,” *Anal. Biochem.* **195**, 330–351 (1991).
5. S. Fantini, M. A. Franceschini, J. S. Maier, *et al.*, “Frequency-domain multichannel optical detector for noninvasive tissue spectroscopy and oximetry,” *Opt. Eng.* **34**, 32–42 (1995).
6. M. Essenpreis, M. Cope, C. E. Elwell, *et al.*, “Wavelength dependence of the differential pathlength factor and the log slope in time-resolved tissue spectroscopy,” in *Optical Imaging of Brain Function and Metabolism*, U. Dirnagl, A. Villringer, and K. M. Einhäuser, eds. (Springer, 1993), pp. 9–20.
7. M. Kohl, C. Nolte, H. R. Heekeren, *et al.*, “Determination of the wavelength dependence of the differential pathlength factor from near-infrared pulse signals,” *Phys. Med. & Biol.* **43**, 1771 (1998).
8. I. Pirovano, S. Porcelli, R. Re, *et al.*, “Effect of adipose tissue thickness and tissue optical properties on the differential pathlength factor estimation for nirs studies on human skeletal muscle,” *Biomed. Opt. Express* **12**, 571–587 (2021).
9. A. Duncan, J. H. Meek, M. Clemence, *et al.*, “Optical pathlength measurements on adult head, calf and forearm and the head of the newborn infant using phase resolved optical spectroscopy,” *Phys. Med. & Biol.* **40**, 295–304 (1995).
10. A. Duncan, J. H. Meek, M. Clemence, *et al.*, “Measurement of cranial optical path length as a function of age using phase resolved near infrared spectroscopy,” *Pediatr. Res.* **39**, 889–894 (1996).
11. S. J. Matcher, C. E. Elwell, C. E. Cooper, *et al.*, “Performance comparison of several published tissue near-infrared spectroscopy algorithms,” *Anal. Biochem.* **227**, 54–68 (1995).
12. T. W. L. Scheeren, P. Schober, and L. A. Schwarte, “Monitoring tissue oxygenation by near infrared spectroscopy (nirs): Background and current applications,” *J. Clin. Monit. Comput.* **26**, 279–287 (2012).
13. F. Scholkmann, A. J. Metz, and M. Wolf, “Measuring tissue hemodynamics and oxygenation by continuous-wave functional near-infrared spectroscopy—how robust are the different calculation methods against movement artifacts?” *Physiol. Meas.* **35**, 717–734 (2014).
14. L. Hou, Y. Liu, L. Qian, *et al.*, “Portable near-infrared technologies and devices for noninvasive assessment of tissue hemodynamics,” *J. Healthc. Eng.* **2019**, 3750495 (2019).
15. J. Zhang, T. Yu, M. Wang, *et al.*, “Clinical applications of functional near-infrared spectroscopy in the past decade: A bibliometric study,” *Appl. Spectrosc. Rev.* **59**, 908–934 (2024).
16. N. Wang, Y. He, S. Zhu, *et al.*, “Functional near-infrared spectroscopy for the assessment and treatment of patients with disorders of consciousness,” *Front. Neurol.* **16** (2025).
17. M. Tuesta, R. Y. nez Sepúlveda, H. Verdugo-Marchese, *et al.*, “Near-infrared spectroscopy used to assess physiological muscle adaptations in exercise clinical trials: A systematic review,” *Biology* **11**, 1073 (2022).
18. J. Corral-Pérez, A. Marín-Galindo, M. Costilla, *et al.*, “Reliability of near-infrared spectroscopy in measuring muscle oxygenation during squat exercise,” *J. Sci. Med. Sport* **27**, 805–813 (2024).
19. M. S. Weingarten, M. Neidrauer, A. Mateo, *et al.*, “Prediction of wound healing in human diabetic foot ulcers by diffuse near-infrared spectroscopy: A pilot study,” *Wound Repair Regen.* **18**, 180–185 (2010).
20. C. Andersen, H.-C. J. Reiter, and V. L. Marmolejo, “Redefining wound healing using near-infrared spectroscopy,” *Adv. Ski. & Wound Care* **37**, 243–247 (2024).
21. T. Talukdar, S. G. Diamond, and J. H. Moore, “Continuous correction of differential path length factor in near-infrared spectroscopy,” *J. Biomed. Opt.* **18**, 056001 (2013).
22. S. L. Jacques, “History of monte carlo modeling of light transport in tissues using mcml.c,” *J. Biomed. Opt.* **27**, 083002 (2022).
23. S. Fantini, D. Hueber, M. A. Franceschini, *et al.*, “Non-invasive optical monitoring of the newborn piglet brain using continuous-wave and frequency-domain spectroscopy,” *Phys. Med. & Biol.* **44**, 1543–1563 (1999).
24. S. R. Arridge, M. Cope, and D. T. Delpy, “The theoretical basis for the determination of optical pathlengths in tissue: temporal and frequency analysis,” *Phys. Med. & Biol.* **37**, 1531–1560 (1992).
25. P. van der Zee, M. Cope, S. R. Arridge, *et al.*, “Experimentally measured optical pathlengths for the adult head, calf and forearm and the head of the newborn infant as a function of inter optode spacing,” in *Oxygen Transport to Tissue XIII*, T. K. Goldstick, M. McCabe, and D. J. Maguire, eds. (Springer US, Boston, MA, 1992), pp. 143–153.
26. D. A. Boas, T. Gaudette, G. Strangman, *et al.*, “The accuracy of near infrared spectroscopy and imaging during focal changes in cerebral hemodynamics,” *NeuroImage* **13**, 76–90 (2001).
27. G. Strangman, M. A. Franceschini, and D. A. Boas, “Factors affecting the accuracy of near-infrared spectroscopy concentration calculations for focal changes in oxygenation parameters,” *NeuroImage* **18**, 865–879 (2003).
28. M. Das, C. Xu, and Q. Zhu, “Analytical solution for light propagation in a two-layer tissue structure with a tilted interface for breast imaging,” *Appl. Opt.* **45**, 5027–5036 (2006).
29. H. Dehghani, M. E. Eames, P. K. Yalavarthy, *et al.*, “Near infrared optical tomography using nirfast: Algorithm for numerical model and image reconstruction,” *Commun. Numer. Methods Eng.* **25**, 711–732 (2009).
30. D. Piao, R. L. Barbour, H. L. Gruber, and D. C. Lee, “On the geometry dependence of differential pathlength factor for near-infrared spectroscopy. i. steady-state with homogeneous medium,” *J. Biomed. Opt.* **20**, 105005 (2015).
31. M. Bhatt, K. R. Ayyalasomayajula, and P. K. Yalavarthy, “Generalized beer–lambert model for near-infrared light propagation in thick biological tissues,” *J. Biomed. Opt.* **21**, 076012 (2016).

32. M. A. Kamran, M. M. N. Mannan, and M. Y. Jeong, “Differential path-length factor’s effect on the characterization of brain hemodynamics using functional near-infrared spectroscopy,” *Front. Neuroinformatics* **12**, 37 (2018).

33. H. Zohdi, F. Scholkmann, N. Nasseri, and U. Wolf, “Long-term changes in optical properties ( $\mu_a$ ,  $\mu'_s$ ,  $\mu_{\text{eff}}$  and dpf) of human head tissue during functional neuroimaging experiments,” in *Oxygen Transport to Tissue XL*, O. Thews, J. C. LaManna, and D. K. Harrison, eds. (Springer International Publishing, Cham, 2018), pp. 331–337.

34. A. Sassaroli and S. Fantini, “Comment on the modified beer-lambert law for scattering media,” *Phys. Med. & Biol.* **49**, N255–N257 (2004).

35. J. S. Ultman and C. A. Piantadosi, “Differential pathlength factor for diffuse photon scattering through tissue by a pulse-response method,” *Math. Biosci.* **107**, 73–82 (1991).

36. S. Chatterjee, T. Y. Abay, J. P. Phillips, and P. A. Kyriacou, “Investigating optical path and differential pathlength factor in reflectance photoplethysmography for the assessment of perfusion,” *J. Biomed. Opt.* **23**, 075005 (2018).

37. M. Kohl, U. Lindauer, G. Royl, *et al.*, “Physical model for the spectroscopic analysis of cortical intrinsic optical signals,” *Phys. Med. & Biol.* **45**, 3749–3764 (2000).

38. J. Gervain, J. Mehler, J. F. Werker, *et al.*, “Near-infrared spectroscopy: A report from the mcdonnell infant methodology consortium,” *Dev. Cogn. Neurosci.* **1**, 22–46 (2011).

39. A. J. Lin, A. Ponticorvo, A. J. Durkin, *et al.*, “Differential pathlength factor informs evoked stimulus response in a mouse model of alzheimer’s disease,” *Neurophotonics* **2**, 045001 (2015).

40. F. Scholkmann, H. Zohdi, N. Nasseri, and U. Wolf, “Absolute values of optical properties ( $\mu_a$ ,  $\mu'_s$ ,  $\mu_{\text{eff}}$  and dpf) of human head tissue: Dependence on head region and individual,” in *Oxygen Transport to Tissue XL*, O. Thews, J. C. LaManna, and D. K. Harrison, eds. (Springer International Publishing, Cham, 2018), pp. 325–330.

41. T. J. Barstow, “Understanding near infrared spectroscopy and its application to skeletal muscle research,” *J. Appl. Physiol.* **126**, 1360–1376 (2019).

42. B. Koirala, A. Concas, A. Cincotti, *et al.*, “Estimation of differential pathlength factor from nirs measurement in skeletal muscle,” *Respir. Physiol. & Neurobiol.* **326**, 104283 (2024).

43. L. F. Ferreira, D. M. Hueber, and T. J. Barstow, “Effects of assuming constant optical scattering on measurements of muscle oxygenation by near-infrared spectroscopy during exercise,” *J. Appl. Physiol.* **102**, 358–367 (2007).

44. F. Scholkmann and M. Wolf, “General equation for the differential pathlength factor of the frontal human head depending on wavelength and age,” *J. Biomed. Opt.* **18**, 105004 (2013).

45. M. Althobaiti, “Estimation of the differential pathlength factor for human skin using monte carlo simulations,” *Diagnostics* **13** (2023).

46. A. M. Chiarelli, D. Perpetuini, C. Filippini, *et al.*, “Differential pathlength factor in continuous-wave functional near-infrared spectroscopy: Reducing hemoglobin cross talk in high-density recordings,” *Neurophotonics* **6**, 035005 (2019).

47. D. Marti, R. N. N. Aasbjerg, P. E. E. Andersen, and A. K. K. Hansen, “Mcmatlab: an open-source, user-friendly, matlab-integrated three-dimensional monte carlo light transport solver with heat diffusion and tissue damage,” *J. Biomed. Opt.* **23**, 121622 (2018).

48. L. Wang, S. L. Jacques, and L. Zheng, “Mcml—monte carlo modeling of light transport in multi-layered tissues,” *Comput. Methods Programs Biomed.* **47**, 131–146 (1995).

49. T. J. Farrell, M. S. Patterson, and B. C. Wilson, “A diffusion theory model of spatially resolved, steady-state diffuse reflectance for the noninvasive determination of tissue optical properties *in vivo*,” *Med. Phys.* **19**, 879–888 (1992).

50. A. Kienle and M. S. Patterson, “Determination of the optical properties of turbid media from a single monte carlo simulation,” *Phys. Med. & Biol.* **41**, 2221–2227 (1996).

51. D. Piao and S. Patel, “Simple empirical master-slave dual-source configuration within the diffusion approximation enhances modeling of spatially resolved diffuse reflectance at short-path and with low scattering from a semi-infinite homogeneous medium,” *Appl. Opt.* **56**, 1447–1452 (2017).

52. H. G. Akarçay, S. Preisser, M. Frenz, and J. Rička, “Determining the optical properties of a gelatin–tio<sub>2</sub> phantom at 780 nm,” *Biomed. Opt. Express* **3**, 418–434 (2012).

53. S. L. Jacques, “Optical properties of biological tissues: A review,” *Phys. Med. & Biol.* **58**, R37 (2013).